Nanoscale

Accepted Manuscript

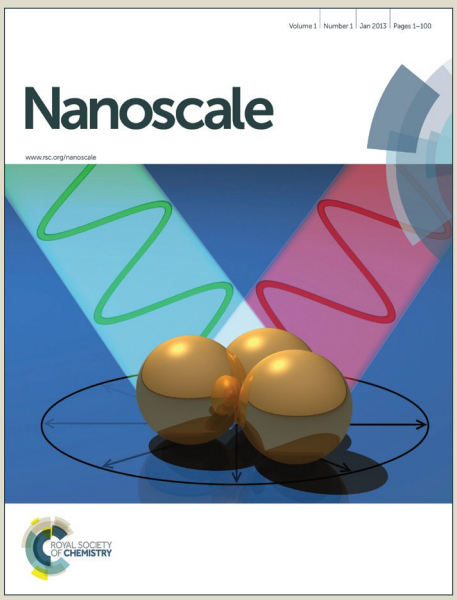

ROYAL SOCIETY OF CHEMISTRY

www.rsc.org/nanoscale

Nanoscale

ARTICLE

Graphene-based large area dye-sensitized solar cell module

Received 00th January 20xx,
Accepted 00th January 20xx

DOI: 10.1039/x0xx00000x

www.rsc.org/

Simone Casaluci[a], Mauro Gemmi[b], Vittorio Pellegrini[c], Aldo Di Carlo[a] and Francesco Bonaccorso†[c]

We demonstrate spray coating of graphene ink as a viable method for large-area fabrication of graphene-based dye-sensitized solar cell (DSSC) modules. A graphene-based ink produced by liquid phase exfoliation of graphite is spray coated onto a transparent conductive oxide substrate to realize a large area (>90cm^2) semi-transparent (transmittance 44%) counter-electrode (CE) replacing platinum, the standard CE material. This is successfully integrated in a large-area (43.2 cm^2 active area) DSSC module achieving a power conversion efficiency (η) of 3.5%. The approach demonstrated here paves the way to all-printed, flexible, and transparent graphene-based large-area and cost-effective photovoltaic devices on arbitrary substrates.

1. Introduction

The development of any photovoltaic (PV) technology is linked to the possibility to scale-up lab-cell prototypes to the proper size required by the specific application. Currently, PV devices are exploited in different contests such as conventional PV plant, building integrated PV (BIPV),[1-3] space solar power,[4,5] energy harvester for sensors and other information and communication technology devices,[6,7] etc. Nowadays, PV technology is largely based on silicon solar cells,[8] showing power conversion efficiency (η), of the order of ~25%.[9] Driven by the need of costs saving,[10] second generation PVs, based on thin film crystalline (c-Si)[11] and amorphous[12] silicon (a-Si), copper indium gallium diselenide,[13] cadmium telluride,[14] have been developed. However, degradation, *e.g.*, a-Si modules suffer the Staebler–Wronski effect,[15] and environmental pollution due to hazardous by-products[16] have pushed the research towards the development of third generation PV cells with the aim to achieve higher η than silicon solar cells by using novel light absorbing materials.[17,18] Meso-super-structured solar cells,[19] based on an organic halide perovskite as photosensitizer,[20] and an organic hole-transport material, [21] with η of 21% have been recently developed.[22] However, despite having easy fabrication techniques,[23] perovskites may not satisfy sustainability requirements, due to their lead content. Another class of PV cells, known as organic PV cells [24] are emerging as a cost effective approach being based on cheaper and more advanced manufacturing processes, e.g., roll-to-roll[25] and other coating/deposition techniques,[26] with respect to the Si technology. *Dye-sensitized solar cell* (DSSC)[27] is another third generation PV technology that have recently achieved η over 14%.[28]

Dye-sensitized solar cell have great potential for large-scale applications, both economically and technically. In fact they demonstrate high η under diffuse light[29] and low illumination conditions,[30] together with the reduced angular dependence of η.[31] Moreover, the possibility to realize DSSCs with on-demand colour and transparency[32] make them well-suited for both indoor applications [33] and BIPVs.[34,35] In this context, although BIPVs based on silicon PV and thin film technologies[36] are largely used in solar park and rooftop applications[37,38] they are not suitable for integration into windows other than shading elements due to the difficulties in tuning color and/or transparency.

A typical DSSC is assembled by placing an electrolyte, either liquid or solid,[39] containing a redox system in between the photoanode, consisting of a high porosity nanocrystalline nanoparticles (*e.g.*, titanium dioxide -TiO_2-, zinc oxide (ZnO),[40] or hybrid materials *e.g.* TiO_2/ZnO [41]) sensitized by dye molecules (photosensitizer of organic[42-44] or inorganic[27,45,46,] nature, see Ref. [47] for a review), and the counter electrode (CE).[27] The latter has a double role; in fact, it back transfers electrons arriving from the external circuit to the redox system[27] and it catalyzes the reduction of the charge mediator.[27] In order to fulfill such functions, the CEs should exhibit high exchange-current density (*i.e.*, the rate of electron transfer between electrolyte and electrode), low charge-transfer resistance –R_{ct}- (*i.e.* the electrode-electrolyte interface resistance), and high specific surface area (SSA).[47]

Counter electrodes are commonly composed by ~15-20 nm thick Pt layer,[27] deposited onto transparent conductor oxides (TCOs) or, more rarely, on stainless steel.[48] However, Pt has several issues. First of all, it has limited reserves on earth and it

[a] CHOSE - Center for Hybrid and Organic Solar Energy, Dept. Electr. Eng. University of Rome "Tor Vergata", via del Politecnico 1, 00133, Rome, Italy.
[b] Center for Nanotechnology Innovation@NEST, Istituto Italiano di Tecnologia, Piazza San Silvestro 12, 56127 Pisa, Italy.
[c] Istituto Italiano di Tecnologia, Graphene Labs, Via Morego 30, 16163 Genova, Italy.
† Email: francesco.bonaccorso@iit.it

is costly.[49] Furthermore, from the technical point of view, Pt suffers degradation over time, especially when in contact with the I_3^-/I^- liquid electrolyte,[50] and it tends to induce formation of polyiodites,[51] strongly reducing the η of DSSCs. The aforementioned issues have given the boost[47,52,53] towards the replacement of Pt with cheaper and/or more stable materials.

In this context, carbon-based nanomaterials have been at the centre of an ongoing research effort for their use as catalyst in DSSCs[54], However, DSSCs based on graphite, [55]carbon nanotubes (CNTs),[48,56] amorphous carbon,[57] and hard carbon spherules (HCS),[55] as catalyst material have, to date, shown η lower than the ones achieved with Pt. Graphene, thanks to its large SSA exceeding $2600 m^2 g^{-1}$,[58] much larger than that reported to date for carbon black (~900 m^2/g [59]) or for CNTs, ≈100-1000 m^2/g, [58] and similar to activated carbon (carbon processed with oxygen to make it porous),[60] high mechanical strength and[61] electrical conductivity (σ)[62] values, can satisfy all the CE requirements. Moreover, the ease of functionalization,[63] together with optical transparency[64] and the potential for mass production,[26] makes graphene an ideal platform for PV applications (*e.g.*, as transparent conductors (TCs),[65] photosensitizers,[66,67] channels for charge transport[68-70]) as well as for other conversion and storage devices.[71]

Graphene-based materials, such as graphene nanoplatelets-GNPs- (sheets of functionalized graphene with an overall thickness ranging from ~2nm to ~15nm),[72] nitrogen-doped GNPs,[73] reduced graphene oxide (RGO)[74-77] and hybrid structures of RGO-GNPs-CNTs[78,79] have been exploited not just to develop Pt-free CEs with results, *i.e., η*, close to or exceeding the ones based on Pt but also to improve the electron transport of photoanode.[80] Indeed, the new record high of DSSCs (η=14.3%) has been achieved exploiting GNPs, in combination with gold and fluorine-doped tin oxide (FTO), at the CE.[28] However, the hybrid structure used (GNP-gold-FTO) for the realization of the CE is based on noble and expensive metal, *i.e.*, gold.[28] Other inorganic layered materials LMs- such as transition metal dichalcogenides (TMDs), transition metal oxide (TMO), and metal carbides, nitrides and sulfides[81] as well as hybrid systems, such as graphene-MoS_2,[82] have been tested as CE in DSSCs however, with *η* lower with respect to state of the art DSSCs.[28] Moreover, the aforementioned materials require both post-processing treatments such as RGO and more costly materials (e.g., CNTs, TMDs and TMOs) with respect to pristine graphite.

Graphene can be produced both by top-down[83-89] and bottom-up[90-94] approaches. However, the latter processes require high temperatures (>1000 °C),[81-84] costly substrates[26] and the additional transfer process to the target substrates.[26] Thus, the top-down approach' is emerging as the most promising one in view of large volume production.[95] In particular, by solution processing it is possible to produce single (SLG) and few-layer (FLG) graphene flakes both starting from oxidized[77,78] and pristine graphite,[83,96] as well as from expanded graphite for the realization of GNPs. Graphene oxide, produced by exfoliation of graphite oxide,[85-87] can be mass-produced at room temperature (RT).[85,86] However, it is insulating,[87] with defects[87] and gap states,[87,97] not offering the optimal charge transfer of electrons arriving from the external circuit to the redox system. Solution processing offers also the possibility to produce other LMs (e.g., TMDs, TMO, etc.)[98] exploiting similar production protocol. Moreover, by solution processing it is possible to produce dispersions[83] and inks,[96,99-102] which can easily be deposited on large area target substrates (by drop casting, filtration[75] and/or printing/coating processes,[91-94] without the need of tedious transfer protocols required by the bottom-up approaches.[26] This is key for the exploitation of graphene in applications where large volume and/or large area films/electrodes are needed.

Here, we demonstrate the printability of graphene inks in dimethylformamide (DMF), on large area TCO (>90 cm^2) by spray coating. Tackling the long lasting issues with the scaling-up from small size cells (~1cm^2) to large area modules, usually associated with a reduction of performances (*i.e.*, η), even more critical in DSSCs[103] due to the management of the liquid electrolyte, we demonstrated the fabrication of large area module (43.2 cm^2 active area) DSSCs based on the large area graphene CE In this work, we designed and fabricated a DSSC Z-type connection module with ad-hoc vertical contacts layout, in term of width and thickness to prevent voltage loss due to large electrical resistance value in the connection of adjacent cells. Moreover, we designed a sealing mask to prevent the corrosion of the vertical metal contacts by the electrolyte. Our DSSC module has achieved an η of 3.5% at 1 Sun, *i.e.*, 100 mW/cm^2. If compared with Pt, our graphene-based ink allows for a cost reduction of ~4 order of magnitudes. Given that material cost and deposition systems play a key role for the development of large area module, the optimization of production/formulation of graphene-based inks and their deposition on both rigid and flexible substrates will enable further the scaling up, thus paving the way to the development of carbon-based DSSC technology.

2. Experimental

2.1. Preparation of graphene ink

The graphene ink used in this work was prepared dispersing 200 mg of Graphite flakes (Sigma Aldrich Ltd.) in 20 ml of DMF (Sigma Aldrich Ltd.). The initial dispersion was then ultrasonicated (Branson 3510) for 6 hours and subsequently ultracentrifuged using a SW-41 swinging bucket rotor in a Beckman-Coulter Optima XPN ultracentrifuge at 20000rpm (~61000g) for 30 mins. After ultracentrifugation, the supernatant was extracted by pipetting.

2.1.1. Characterization of graphene ink

The concentration of graphitic flakes in the as-prepared ink was determined from the absorption spectrum, as described in Ref. [83]. Absorption measurements were carried out with a Jasco V-550 UV-Vis. The viscosity of the ink was measured with a Discovery HR-2 Hybrid Rheometer (TA instruments), using a double-wall concentric cylinders geometry (inner diameter of 32 mm and outer diameter of 35 mm), designed for low-viscosity fluids. The temperatures of the graphene ink and the

DMF solvent were set and maintained at 25°C throughout all the measurements.

For Raman measurements, the graphene ink was diluted with DMF and drop-casted onto a Si wafer with 300nm thermally grown SiO_2. Raman measurements were carried out with a Renishaw 1000 at 532nm and a 100X objective, with an incident power of ~1mW. The D, G and 2D peaks were fitted with Lorentzian functions.

The as-prepared ink was also drop casted at RT onto carbon coated copper TEM grids (300 mesh) and rinsed with DI water. TEM images were taken with a Zeiss Libra 120 transmission electron microscope, operated at 120kV and equipped with an in-column omega filter. All the images and the diffraction patterns were energy filtered with a 15eV slit on the zero loss peak.

2.2. Counter-electrodes fabrication via spray coating graphene ink

Graphene flakes dispersed in DMF were sprayed (N_2 gas carrier) onto TCO (FTO coated glass 2.2 mm thick, 8Ω/□, 25mm × 25mm) substrate. The small area CE was 25 mm × 25 mm, while large area CE 84 mm × 110 mm. During the deposition, the substrate temperature was heated at 100°C, the distance between substrate and aerograph was approximately 15cm and the ink flux was continued during the deposition. The amount of graphene ink deposited onto FTO was 0.5 ml/cm^2. The substrate was then transferred under inert atmosphere (N_2) for annealing at 400°C for 60min. For the PT-based CE, we deposited the Pt paste (Chimet) by screen printing onto the FTO.

2.2.1. Counter-electrodes characterization

The as prepared electrodes were characterized by optical absorption and Raman spectroscopies. Transmittance measurement were carried out by a Shimadzu UV-Vis 2550 spectrophotometer coupled to an integrating sphere. Raman measurements were instead carried out in the same experimental conditions reported for the characterization of the inks, see Sect. 2.1.1.

2.3. Dye sensitizer solar cell and symmetry dummy cell fabrication

To test the performance of graphene flakes as CE in small area devices, we fabricated the DSSC as follow. The photoanodes were realized stamping onto the TCO (see detail in sect. 2.2) a TiO_2 paste (18 NR-T, Dyesol) with a dry thickness, measured via profilometer (Dektak Veeco 150), of 6-7µm (active area 5mm × 5mm). The as produced photoanodes were first left to dry in oven at 90°C and then sintered at 480°C and afterward immerged in a 0.3mM N719 Dye ethanol solution. The graphene-based CE was fabricated following the procedure detailed in Sect. 2.2. The solar cell chamber, resulting from the sandwiching of the photoanode and CE, was filled with the I_3^-/I^- electrolyte EL-HPE (Dyesol).

For EIS measurements we fabricated a symmetric dummy cell. We used two identical CEs made of TCO substrates (details specified in sect. 2.2) covered with both graphene nanoflakes and Pt (see section 2.2 for details) and sealed with thermoplastic resin (25µm thick Surlyn, Solaronix). The I_3^-/I^- electrolyte (HSE- electrolyte, Dyesol) was then filled in between the two symmetric CEs. The active area of 1.44 cm^2 and 0.25 cm^2 was realized cutting a square of thermoplastic mask for the graphene and Pt CEs, respectively. The measurements are carried out at RT, in dark and at bias voltage of 0V.[104,105]

2.4. Module fabrication

We used 2.2 mm-thick FTO/glass substrates (Pilkington, 8 Ω/□) both as the photoanode (84mm × 100mm) and CE support (84mm × 110mm). The substrates after cleaning with ethanol and acetone were scribed by a CO_2 Laser System, Universal Laser System to separate a single cell of module. Dupont 7713 silver paste was deposited via screen printing for the realization of the interconnections between the cells forming the module. The CE glass after drying at 90°C in oven for 15 min, was sintered in oven at 480° for 30min. On the photoanode glass after drying at 90°C in oven, instead we deposited via screen printing technique 8 cells (single cell area 5.4cm^2, 6mm in width and 90mm in length, resulting in a total active area of 43.2cm^2) of TiO_2 paste (20nm sized TiO_2 particles, Dyesol 18 NR-T). The photoanode substrate was dried in oven at 80°C followed by sintering at 480°C for 30min. The TiO_2 layer thickness was measured via profilometer (Dektak Veeco 150) resulting ~6-7µm thick. The nanoporous TiO_2 was sensitized by immersing it in a N719 0.3mM ethanol dye solution at RT. Bynel foils 60µm thick (Solaronix) were used to sealing a module and electrolyte EL-HPE (Dyesol) or EL-HSE (Dyesol) was injected through the hole, in the surlyn mask, on the short edge of each cell, which was subsequently sealed with a resin. The Pt-based reference DSSC module was fabricated following the procedure outlined above, with the only difference relying in the deposition of the Pt paste (Chimet) carried out by screen printer after the deposition and curing of the Ag interconnection. The as-prepared CE was then cured at 480°C for 30min.

2.5. Characterization

The photovoltaic performance of all devices was measured under a Class B Sun Simulator (Solar Constant 1200 KHS) at AM 1.5, 100 mW/cm^2 and 17 mW/cm^2 calibrated with a Skye SKS 1110 sensor, using a Keithley 2420 as a source-meter in ambient condition. The sun simulator is class B in the visible and near-infrared range (class B between 700–800 nm and class A in the rest of the 400–1100 nm range) and has a spatial uniformity <±5%. Sun simulator spectrum was measured with a BLACK-Comet UV-VIS Spectrometer (range 190-900 nm).

For EIS measurement to investigate the Rct of electrolyte/catalytic interface we utilized AUTOLAB 302N potentiostat (Metrohm) and Nova electrochemical interface system with all measurements carried out in dark at 0V and at RT. The frequency was in the 20Hz-1MHz range and the amplitude of the a.c. voltage was 10mV.

3. Results and discussion

Graphene-based ink is prepared via low-power ultrasonication of graphite in DMF. The choice of graphite exfoliation in DMF is set by the need of having the best contact at the inter-flake junctions upon deposition on the electrode, which could be affected by the surfactant coverage in aqueous solutions,[106,107] and by the lower boiling point (153°C)[108] with respect to N-Methyl2Pyrrolidone (202°C).[109] The ultrasonication process induces exfoliation of the graphitic flakes[83] producing a heterogeneous dispersion of thin/thick and small/large graphitic flakes.[26]

We exploit sedimentation-based separation (SBS) to sort graphitic flakes by lateral size.[88] The rate of sedimentation of a graphitic flake in a centrifugal field is described by the Svedberg equation:[110]

$$s=v/\omega^2 r=m(1-\acute{u}\rho)/f \quad (1)$$

with s the sedimentation coefficient reported in Svedberg (S) unit (1S corresponds to 10^{-13} sec.),[110] m the mass, ú the partial specific volume (the volume that each gram of the graphitic flake occupies in solution), ρ the density of the solvent and f the frictional coefficient which depends on the morphological properties (lateral size and thickness) of the graphitic flakes and the viscosity of the solvent. In general, f increases as the particle geometry moves away from a spherical shape, which means that large or elongated particles experience more frictional drag than compact, smooth spherical ones.[88,128] s depends on the morphological properties of the particle and is proportional to the buoyant effective molar weight of the particle, while it is inversely proportional to f.[110] As reported in Eq. 1, the sedimentation of graphitic flakes depends on the frictional coefficient and mass.[26,88] Thick and large flakes, having larger mass, sediment faster with respect to thin and small flakes (having smaller mass), which are thus retained in dispersion.

3.1. Characterization of graphene-based ink

The rheological properties of the as-formulated inks were characterized by means of optical absorption spectroscopy (OAS) and viscosity measurements under shear conditions. We use OAS in order to evaluate the concentration (c) of graphitic material in the ink.

Figure 1a plots the OAS of the ink prepared via SBS. The UV absorption peak at ~266nm is attributed to inter-band electronic transitions from the unoccupied π* states at the M point of the Brillouin zone.[111,112] The asymmetry of the UV peak, with a high-wavelength tail, is attributed to excitonic effects.[112,113] Using the experimentally derived absorption coefficient of 1390 $Lg^{-1}m^{-1}$ at 660 nm[83] we estimate c ~60 mg/L. Concerning the viscosity of our ink, the inset to Figure 1a shows the viscosity of the ink, as well as the one of the pure DMF for comparison, under shear stress. The ink has ν = 1.02 mPa s, which is only ~8% higher than the solvent one (0.93 mPa s),[114] probably due to the low concentration (c ~60 mg/L) of the graphene-ink. The viscosity of the graphene-based ink, as well as the pure DMF, is almost independent of the shear rate, at least in the shear rate range here investigated, a behaviour typical of Newtonian fluid (*i.e.*, a fluid in which the viscosity arising from its flow is linearly proportional to the strain rate, such as water and solvents).[115]

The morphological properties of the graphene flakes dispersed in the ink are characterized by means of transmission electron microscopy (TEM) and Raman spectroscopy.

Figure 1 b) plots a low-resolution TEM bright field image of a flake deposited on the TEM grid. The sample is formed by flakes having average dimensions in the range ~0.01–0.02 μm^2. Electron diffraction collected on flake aggregates shows polycrystalline rings demonstrating that the flakes are crystalline. All the rings can be indexed as h,k,-h-k,0 reflections of an hexagonal lattice with a=0.244(1)nm, in agreement with the graphene structure.[116]

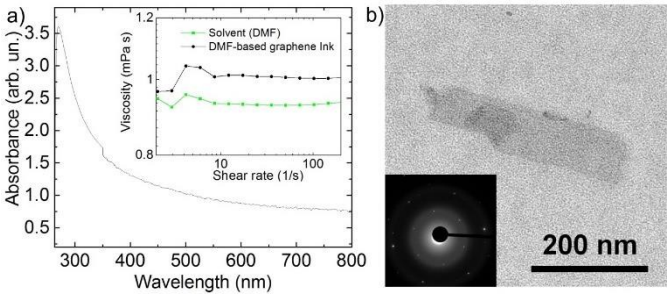

Figure 1 (a) Room temperature absorption spectrum of the SBS graphene ink. Inset: viscosity of the produced inks vs shear rate for DMF (green curve) and DMF-graphene ink (black curve). (b) Bright field TEM images of a graphene flake at low magnification. Inset: Electron diffraction pattern collected on an area of 2 μm in diameter. The 10-10 and 11-20 polycrystalline diffraction rings of graphene are clearly visible. The rings are formed by strong spots corresponding to the larger flakes and a background of weaker unresolved spots associated with smaller flakes.[117]

Raman spectroscopy is a fast and non-destructive technique to identify number of layers, doping, defects, disorder, chemical modifications and edges of graphitic flakes.[117,118] In a typical Raman spectrum of graphene, the two main peaks are the G peak, corresponding to the E_{2g} phonon at the Brillouin zone centre,[117,118] and the D peak, which is due to the breathing modes of sp^2 rings and requires a defect for its activation by double resonance. The 2D peak is the second order of the D peak, being a single peak in monolayer graphene, whereas splitting in four components in bi-layer graphene, thus reflecting the evolution of the band structure. Because no defects are required for the activation of two phonons with the same momentum, one backscattered from the other, the 2D peak is always seen, even in the absence of D peak.

Double resonance can also happen as an intra-valley process, *i.e.* connecting two points belonging to the same cone around K or K',[117] giving rise to the D' peak. The 2D' is the second order of the D', and as in the case of the 2D peak is always seen, even in the absence of D' peak.

Statistical analysis of the micro-Raman spectra (Figure 2a) shows that the 2D peak is at Pos(2D) ~2691cm^{-1} (Figure 2b), while the FWHM(2D) varies from 60 to 95cm^{-1} with a peak at ~80cm^{-1} (Figure 2c) and I(2D)/I(G) varies from 0.75 to 1.30 (Figure 2d). This is consistent with the sample being a combination of SLG and FLG flakes. The Raman spectra show significant D and D' peaks intensity, with an average intensity ratio I(D)/I(G) ~1.50 (see Figure 2e) and I(D')/I(G) ~0.35. This is attributed to the edges of our nanometer flakes, rather than to structural defects on the basal plane of SLG and FLG flakes.

This observation is supported by the analysis of I(D)/I(G) (Figure 2e), FWHM(G) (Figure 2f) and Pos(G) (Figure 2g). Indeed, combining I(D)/I(G) with FWHM(G) allows us to discriminate between disorder localized at the edges and disorder in the bulk. In the latter case, a higher I(D)/I(G) would correspond to higher FWHM(G). I(D)/I(G) and FWHM(G) are not correlated, as shown Figure 2h, an indication that the major contribution to the D peak comes from the sample edges. Moreover, in the high-defect concentration regime FWHM(G) and FWHM(D') become broader and eventually merge into a single band[117].

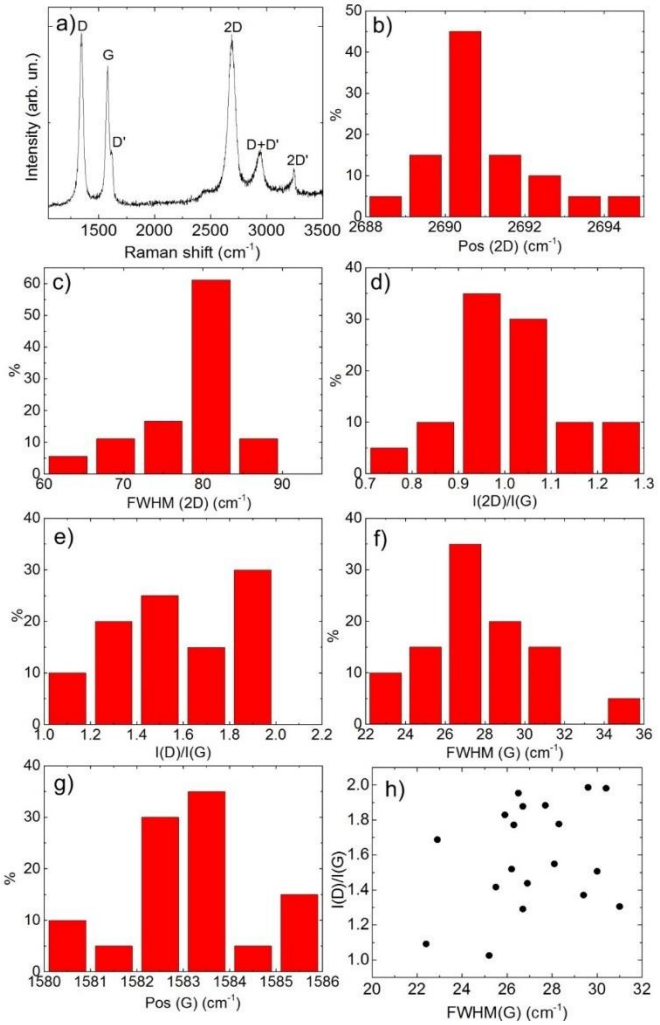

Figure 2 (a) Raman spectra of graphene inks in DMF. (b-h) Statistic of Raman analysis of graphene ink. Distribution of b) Pos(2D), c) FWHM(2D), d) I(2D)/I(G), e) I(D)/I(G), f) FWHM(G), g) Pos(G) and h) I(D)/I(G) as a function of FWHM(G).

3.2. Counter-electrodes

Graphene flakes are then deposited on FTO substrates (see Methods for details) by spray-coating (Figure 3a), a technique widely used for depositing thin films on a substrate.[119] This technique is widely used in the industrial coating, painting and graphic arts,[120] and it has been also exploited to fabricate RGO-based transparent conductive film.[121] In the spray deposition process, the overall quality of the coating is determined both by the rheological properties of the ink such us density, surface tension and viscosity, as we have discussed before for the characterization of our ink, and by other process parameters, such as the spray pressure and distance to the sample, spray time and temperature, as well as the substrate physical chemical characteristic.[119]

We deposited graphene ink in DMF on FTO substrate kept at a temperature of 100°C, as shown in Figure 3a (see methods for more details). Considering a concentration of 60mg/L for our graphene ink, see Fig. 1a, we can estimate a loading of graphene flakes of ~30μg/cm^2 onto the CE. After the deposition is completed, the substrate is thermally treated at 400°C for 60min, under N_2 atmosphere. The as-produced graphene-based CEs (see Figure 3b) are then characterized by absorption and Raman spectroscopy. Figure 3c shows that the fabricated graphene-based CE has a transmittance of ~43% including the FTO substrate (transmittance FTO ~80%) at 550nm. Note that the commonly used wavelength for the optical characterization of transparent conductors is 550nm where the human eye is most sensitive.[64] This transmittance value renders the CE semitransparent, as demonstrated by the photograph in Figure 3b.

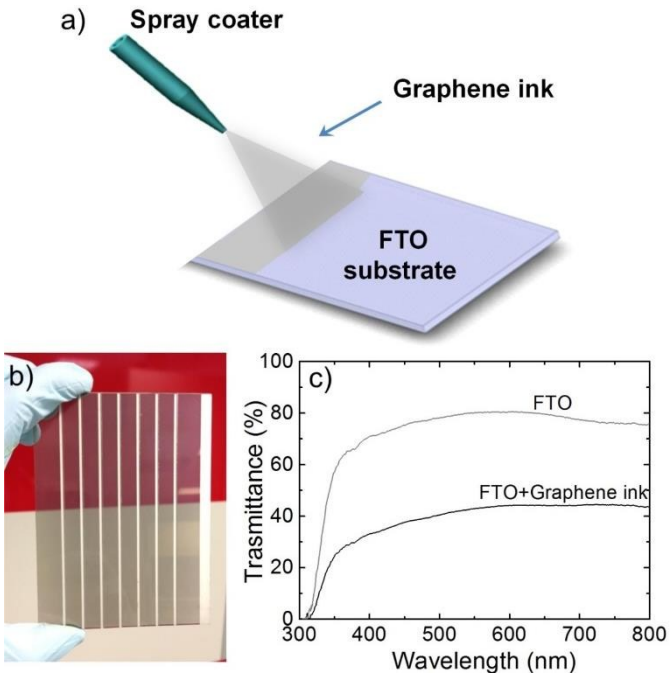

Figure 3 a) Spray coating graphene ink. The graphene ink is deposited through the air onto the FTO substrate by a spray gun. b) Optical image of graphene-counter electrode. c) Optical transmittance of FTO (grey curve) and graphene-coated FTO substrate (black curve).

The as-produced CE is also characterized by Raman spectroscopy in order to monitor the quality of the flakes composing the CE. Figure 4a compares a typical Raman spectrum measured at 532nm for a flake deposited onto SiO_2 substrate from the ink, with that of the graphene-FTO electrode. Figure 4b-e compare Pos(2D) and FWHM(2D) distributions. The graphene-FTO electrode has a larger distribution of both Pos(2D) (between ~2692 cm^{-1} and ~2702 cm^{-1}) and FWHM(2D) (peak at ~80 cm^{-1}), with respect to the graphene flakes. However, the 2D peak still shows a Lorentzian lineshape distinctly different from that of graphite. This implies that the flakes are SLG or, if FLG, they are electronically almost decoupled and behave, to a first approximation, as a collection of SLGs.

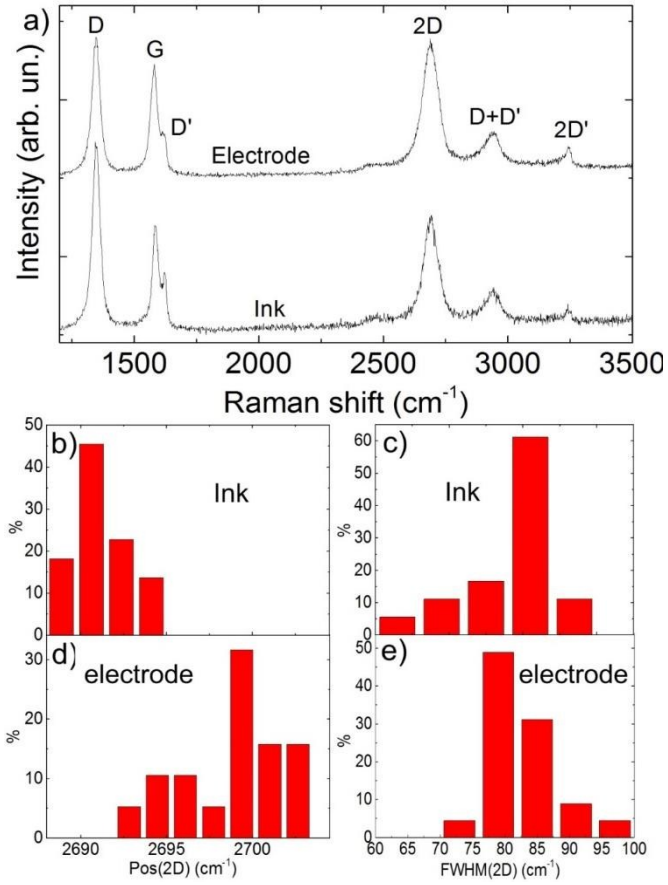

Figure 4 a) Representative Raman spectrum of flakes dispersed in the ink, compared with the spectrum taken on the glass substrate. Pos(2D) and FWHM(2D) for (b, c) flakes in the ink and (d, e) spray deposited on the FTO substrate.

3.3. Electrochemical properties

Electrochemical impedance spectroscopy (EIS), *i.e.*, the measurement of the linear electrical response for the evaluation of the physico-chemical properties of the electrochemical system under investigation, is exploited to evaluate/quantify the catalytic activity of DSSC CEs and carried out in dummy cell configuration (see section 2.3 for details and Figure 5a for a schematic representation). In such configuration, a thin layer of electrolyte solution is sandwiched between two identical electrodes to be tested as DSSC CEs. The symmetrical dummy cell configuration permits to investigate both the electrochemical activity and stability of a CE, under simulated DSSC operating conditions, but with the advantage of eliminating the photoanode contribution.[104,122,123, 124]

Electrochemical impedance spectroscopy data are represented by a complex plane (Nyquist plot) that includes the imaginary impedance (Y-axes) that represents the capacitive and inductive behaviour of the cell against the real impedance (X-axes). In the plot, each point represents the impedance value at a defined frequency (data associated to low frequency scan are reported on the right side of the plot while the ones associated to higher frequency are on the left part).[125-127] Typically, a Nyquist plot of the symmetrical dummy cell exhibits two semicircles.[127] The first one at high frequency (KHz-MHz range) is attributed to the catalyst/electrolyte interface,[125] while the second one, shifted toward lower frequency (Hz range), is linked with ionic diffusion processes in the electrolyte.[125]

The Nyquist plot of our symmetrical dummy cell (see Fig. 5b), composed by I_3^-/I^- liquid electrolyte sandwiched in between two graphene-based electrodes, measured in the 20Hz-1MHz range, displays the first semicircle. The width of this semicircle, along X-axes, give indication about the R_{ct} (*i.e.* the electrode-electrolyte interface resistance). Large semicircle is synonymous of large R_{ct} value and vice-versa.[128] The intercept with the X-axis of the first semicircle represents R_s, the ohmic resistance of electrolyte and the resistance of external circuit included TCO resistance,[143,128] here estimated to be ~18 Ω.

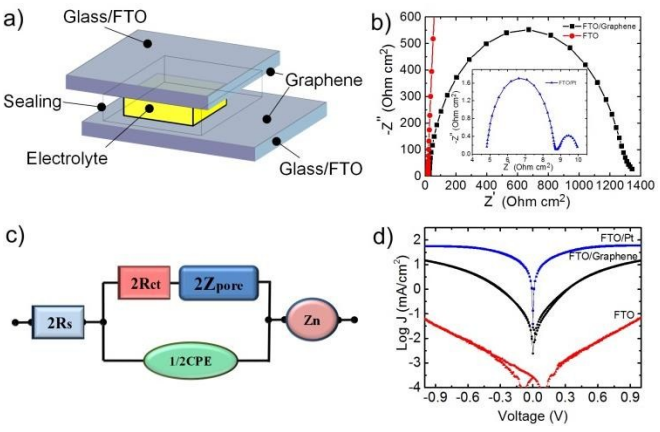

Figure 5 a) Schematic of dummy cell for EIS measurements. b) Nyquist plots of FTO (red line) and FTO-graphene (black line) CEs measured in the 20Hz-1MHz range. In the inset is reported the EIS plot of dummy cell fabricated with Pt CE. (c) Equivalent circuit used for data fitting. d) Tafel plot for dummy cell assembled with FTO, FTO/Graphene and FTO/Pt.

The scheme of the circuit used for the determination of Rct is shown in Fig.5c. Here, CPE represents the constant phase element associated with the CE-electrolyte interface, describing deviation from the ideal capacitance,[128] Zn represents the Nernst diffusion impedance of triiodide in the electrolyte solution,[128] while Zpore is the Nernst diffusion

impedance in the pores of the electrode material.[75] The parameter Zpore was introduced for functionalized graphene contacting an I_3^-/I^- electrolyte solution.[75] However, to this parameter is associated a third semicircle at high frequency on Nyquist plot, which we do not detect in our measurements and consequently it was neglected.[128] A performant CE should have both low R_{ct} and high catalytic activity.[129] The inset to Fig. 5b shows the EIS plot for a dummy cell fabricated with Pt (R_{ct}= 2 Ω·cm^2). A large value of R_{ct} (> 10 kΩ·cm^2) measured for the CE made of only FTO is a clear fingerprint of its poor catalytic activity.[130] After the spray deposition of the graphene ink, we have not detected any change in the Rs value (~18 Ω), while, on the contrary, we have seen that R_{ct} decreased to 650 Ω·cm^2, with respect to the value of FTO CE. As reported in literature,[122] graphene-based CEs (*i.e.*, GNPs) have shown low catalytic activity with iodide-based electrolyte if compared with the case of cobalt based mediator.[122] The low catalytic activity of graphene-based CE with iodide-based electrolyte is highlighted by the high R_{ct}, which is reflected with low FF in solar cell devices under strong illumination condition.

To better understand the electrochemical activity of the CE/mediator interface, in Fig. 5d we show the Tafel plot, a logarithmic current density (J) as a function of voltage for the dummy cells with (FTO/graphene) and without (FTO) graphene and compared with the one with Pt (FTO/Pt), used as reference. In the curve at high potential (horizontal part), it is possible to derive the limiting diffusion current density (J_{lim}). J_{lim} is determined by the diffusion properties of the redox couple and the activity of the CE catalysts.[131] Fig. 5d shows a poor catalytic activity of the FTO-based CE. Contrary, graphene-flakes spray deposited onto FTO substrate shows a catalytic activity towards the redox system, producing a J_{lim} of 14.9 mA/cm^2. However, this value is still lower with respect to the one of FTO/Pt CE (60.5 mA/cm^2). The latter suggests a higher diffusion coefficient (D) compared to that of graphene CE according with equation (2):

$$D = (l/2nFC)J_{lim} \quad (2)$$

where *l* is the spacer thickness of dummy cell, n is the number of electrons involved in the reduction of triiodide at the electrode, F is the Faraday constant, and C is the triiodide concentration.[132] However, more work is still needed to fully understand the catalytic properties of graphene with the I_3^-/I^- charge mediator.

3.4. Photo-electrochemistry performance

The performance of graphene ink on DSSC CE is first tested on a small area (0.25 cm^2) device to monitor the feasibility of the process, namely to test the catalytic activity of graphene flakes before scaling up the device to solar module. The small area DSSC fabrication process is reported in section 2.3. We have tested the DSSCs under two illumination conditions (1 Sun and 0.17 Sun=17 mW/cm^2). In Figure 6 (left side axis) we report the J/V curve at 1 Sun, achieving η=3.6%, open circuit voltage (Voc)= 711 mV, short current density (Jsc)= 14.8 mA/cm^2 and FF= 34.7%. The large Rct value (650 Ω·cm^2) of graphene-based CE influences the J-V shape close to the Voc showing a S-shape characteristic which affects the FF and consequently the η. However, such S-shape characteristic is reduced in low light conditions, *i.e.*, 0.17 sun (right side axis of Figure 6) that have shown better photovoltaic performances, if compared with the ones at 1 sun, with η=4.9%, Voc= 670 mV, Jsc= 2.4 mA/cm^2 and FF= 51.6%, respectively. As reported in literature,[33] the DSSC technology present better performances (*i.e.*, FF and η values) at low lighting illumination conditions. Although Jsc generally decreases at low illumination due to lower photo-generated current and Voc subsequently decrease logarithmically, both the FF and η values increase as a result of the reduction of charge recombination rate.[133] In our case, the S-shape behaviour is less marked at 0.17 Sun with respect to the full illuminated condition (1 Sun), because the photo-generated current can be better sustained by the catalytic properties of the graphene flakes, in agreement with the electrochemical results reported in the previous section.

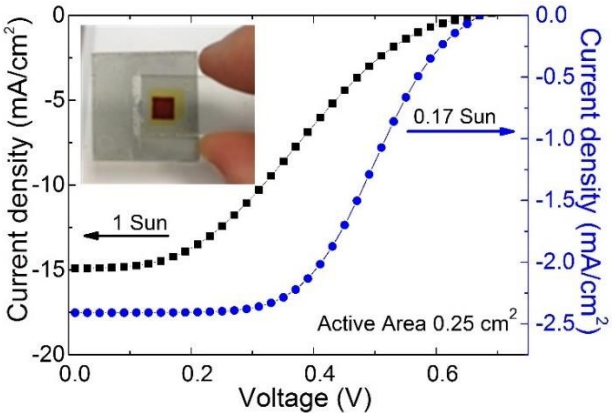

Figure 6 J-V curve of small area device (0.25 cm^2). Graphene flakes on CE were deposited by spray coating. In the inset a picture of assembled device.

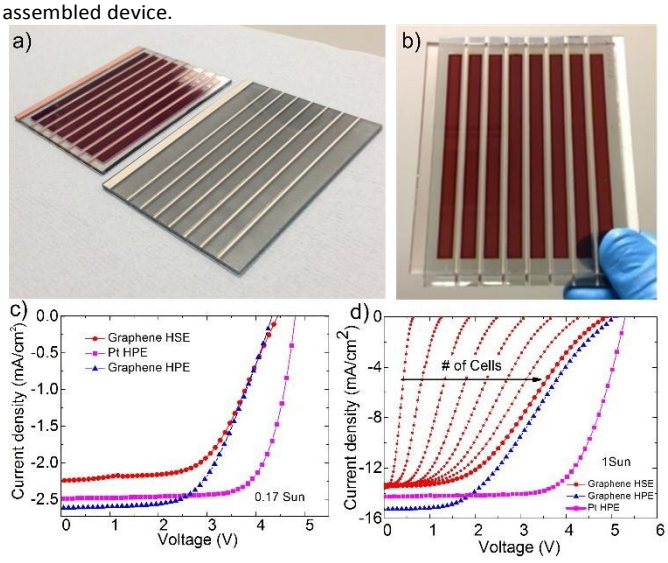

Figure 7 Large area module and J-V curves. Photographs of a) photoanode and graphene-based CE and b) complete large area DSSC module. c) J-V curve of DSSC modules with Pt CE (violet curve) and graphene-based CE with different electrolytes (HSE red curve and HPE blue curve) tested at 17mW/cm^2. d) J-V curve of the same modules reported in c) illuminated at 100mW/cm^2; the contribution each cell composing the module is reported for graphene-based CE and HSE electrolyte.

Several strategies have been proposed to improve the catalytic properties of the graphene ad consequently to reduce the S-shape behaviour such as graphene on a Ni nanoparticles-based layer [134] and graphene with Pt nanoparticles.[135] In the following, however, we will focus only on pristine graphene flakes being promising for indoor applications and avoiding, at the same time, possible instabilities of the catalysts due to the presence of Ni or Pt nanoparticles.[51]

Having tested the photovoltaic and electrochemical performances of our graphene flakes-based ink, we now demonstrate the scalability of our approach to printed large-area modules. Figure 7a reports a photograph of the photoanode module, left side, with sensitized active area and silver vertical contact. On the right side of the photograph, the CE module after the spray coating deposition of the graphene flakes-based ink. Figure 7b shows the sandwich-type assembled module comprising the photoanode and CE (>90 cm^2) substrate. The Figure 7c and Figure 7d show the J-V curves of large area DSSC module at different illumination conditions (1 Sun and 0.17 Sun). We compare the photovoltaic performance of a module fabricated with Pt (used as reference), with those fabricated with graphene ink as CE. We considered two different iodide-based electrolytes, namely the High Stability Electrolyte (HSE, Dyesol) able to guarantee the time stability of solar cell[136] and the High Performant Electrolyte (HPE, Dyesol) able to guarantee high performance, *i.e.* η, of the solar cell.[137] Although the Jsc value is typical for this dye/electrolyte combination[137] as expected, (see Figure 7c and Figure 7d) the module with HPE outperform the one with HSE. However, the increase of the η is dependent on the light intensity: at 1 sun the module with HPE has a 6% larger efficiency value than the HSE one, while at 0.17 sun it is 14% larger. In particular, Figure 7d shows the J-V curve of single cells of module fabricated with HSE where all the single cells, and the complete module curve, have the same short-circuit current (13.4 mA/cm^2) confirming a good uniformity of the module's fabrication which prevent the unbalance in term of current of the module itself. All the photovoltaic parameters are summarized in table 1.

Table 1 Photovoltaic parameters for large area DSSC (43.2 cm^2) with counter electrode made with Pt as reference, and graphene ink using electrolyte EL-HSE and EL-HPE.

Large area module (43.2 cm^2)						
Counter electrode material	Electrolyte	Illumination intensity (mW/cm^2)	η (%)	Voc (V)	Jsc (mA/cm^2)	FF (%)
Pt	HPE	100	6.3	5.3	14.3	67.4
		17	6.4	4.8	2.5	73.1
Graphene	HPE	100	3.5	4.9	15.2	38.8
		17	4.8	4.3	2.6	58
Graphene	HSE	100	3.3	4.9	13.4	39.8
		17	4.2	4.4	2.2	57.6

We notice that, for the same electrolyte (HPE) the J_{SC} of graphene-based module is larger than the one with Pt, confirming the potentiality of graphene as catalyst for large area DSSC modules. In particular, taking into account the performance/cost ratio, the replacement of Pt with graphene flakes may result in ~four orders of magnitude cost reduction (the costs are for materials only and based on Sigma-Aldrich values available at www.sigmaaldrich.com), which coupled with the easy deposition method will enable further the scaling up, thus paving the way to the development of carbon-based DSSC technology.

4. Conclusions

We demonstrated a large-area dye-sensitized solar cell module based on spray-coated graphene ink counter electrode. We produced a graphene-based ink by liquid phase exfoliation of graphite in Dimethylformamide. By using spray coating we deposited the graphene ink on a transparent conductive oxide substrate to realize a large area (~90 cm^2) counter-electrode with a transparency of 44%. The large area (43.2 cm^2 active area) dye-sensitized solar cell module achieved an η of 3.5%. In view of performance/cost ratio of photovoltaic devices, the exploitation of graphene ink can be a viable alternative to current technology based on Pt. Moreover, the use of cobalt-based mediator could boost the performances of DSSC modules, as already demonstrated for lab-scale DSSC devices. Further optimization of graphene-based inks formulation and their deposition methods on both rigid and flexible substrates, will pave the way to all-printed, flexible, and transparent graphene-based photovoltaic devices on arbitrary substrates.

Acknowledgements

The research leading to these results has received funding from the European Union Seventh Framework Programme under grant agreement n°604391 Graphene Flagship.

References

1. B. Norton, P. C. Eames, T. K. Mallick, M. J. Huang, S. J. McCormack, J. D. Mondol and Y. G. Yohanis, *Solar Energy*, 2011, **85**, 1629-1664.
2. Y. T. Chae, J. Kim, H. Park and B. Shin, *Applied Energy*, 2014, **129**, 217-227.
3. A. Nathan, A. Ahnood, M. T. Cole, S. Lee, Y. Suzuki, P. Hiralal, F. Bonaccorso, T. Hasan, L. Garcia-Gancedo and A. Dyadyusha et al., *Proceedings of the IEEE*, 2012, **100**, 1486-1517.
4. R. Hoheisel, S. R. Messenger, M. P. Lumb, M. Gonzalez, C. G. Bailey, D. A. Scheiman, S. Maximenko, P. P. Jenkins and R. J. Walters, 2013.
5. S. Bailey and R. Raffaelle, in *Handbook of Photovoltaic Science and Engineering*, John Wiley & Sons, Ltd, 2011, DOI: 10.1002/9780470974704.ch9, pp. 365-401.
6. F. Bonaccorso and Z. Sun, Opt. Mater. Express 2014, 4, 63-78.

7. G. Fiori, F. Bonaccorso, G. Iannaccone, T. Palacios, D. Neumaier, A. Seabaugh, S. K. Banerjee and L. Colombo, *Nat Nano*, 2014, **9**, 768-779.
8. D. M. Chapin, C. S. Fuller and G. L. Pearson, *J. Appl. Phys.*, 1954, **25**.
9. M. A. Green, K. Emery, K. Bücher, D. L. King and S. Igari, *Progress in Photovoltaics: Research and Applications*, 1999, **7**, 321-326.
10. L. M. Peter, *Philosophical Transactions of the Royal Society of London A: Mathematical, Physical and Engineering Sciences*, 2011, **369**, 1840-1856.
11. A. Goetzberger, C. Hebling and H.-W. Schock, *Materials Science and Engineering: R: Reports*, 2003, **40**, 1-46.
12. D. E. Carlson and C. R. Wronski, *Appl. Phys. Lett.*, 1976, **28**, 671-673.
13. L. L. Kazmerski, F. R. White and G. K. Morgan, *Appl. Phys. Lett.*, 1976, **29**, 268-270.
14. J. Lebrun, 1970.
15. D. Staebler and C. Wronski, *J. Appl. Phys*, 1980, **51**, 3262-3268.
16. A. Yassin, F. Yebesi and R. Tingle, *Environ. Health Perspect.*, 2005, 255-260.
17. H. Hoppe and N. S. Sariciftci, *J. Mater. Res.*, 2004, **19**, 1924-1945.
18. A. S. Polo, M. K. Itokazu and N. Y. M. Iha, *Coord. Chem. Rev.*, 2004, **248**, 1343-1361.
19. A. Kojima, K. Teshima, Y. Shirai and T. Miyasaka, *J. Am. Chem. Soc.*, 2009, **131**, 6050-6051.
20. M. Liu, M. B. Johnston and H. J. Snaith, *Nature*, 2013, **501**, 395-398.
21. F. Di Giacomo, S. Razza, F. Matteocci, A. D'Epifanio, S. Licoccia, T. M. Brown and A. Di Carlo, *J. Power Sources*, 2014, **251**, 152-156.
22. http://www.nrel.gov/ncpv/images/efficiency_chart.jpg, (Accessed: January, 2016).
23. S. Casaluci, L. Cinà, A. Pockett, P. S. Kubiak, R. G. Niemann, A. Reale, A. Di Carlo and P. Cameron, *J. Power Sources*, 2015, **297**, 504-510.
24. W. Tress, in *Organic Solar Cells*, Springer, 2014, pp. 67-214.
25. F. C. Krebs, *Org. Electron.*, 2009, **10**, 761-768.
26. F. Bonaccorso, A. Lombardo, T. Hasan, Z. Sun, L. Colombo and A. C. Ferrari, *Mater. Today*, 2012, **15**, 564-589.
27. B. O'regan and M. Grätzel, *nature*, 1991, **353**, 737-740.
28. K. Kakiage, Y. Aoyama, T. Yano, K. Oya, J.-i. Fujisawa and M. Hanaya, *Chem. Commun.*, 2015, **51**, 15894-15897.
29. C. Cornaro and A. Andreotti, *Progress in Photovoltaics: Research and Applications*, 2013, **21**, 996-1003.
30. N. Sridhar and D. Freeman, 2011.
31. D. D'Ercole, L. Dominici, T. M. Brown, F. Michelotti, A. Reale and A. Di Carlo, *Appl. Phys. Lett.*, 2011, **99**, 213301.
32. R. Tagliaferro, D. Colonna, T. M. Brown, A. Reale and A. Di Carlo, *Opt. Express*, 2013, **21**, 3235-3242.
33. F. De Rossi, T. Pontecorvo and T. M. Brown, *Applied Energy*, 2015, **156**, 413-422.
34. S. Yoon, S. Tak, J. Kim, Y. Jun, K. Kang and J. Park, *Building and Environment*, 2011, **46**, 1899-1904.
35. A. Reale, L. Cinà, A. Malatesta, R. De Marco, T. M. Brown and A. Di Carlo, *Energy Technology*, 2014, **2**, 531-541.
36. S. Strong, *Whole building design guide*, 2010.
37. C. De Castro, M. Mediavilla, L. J. Miguel and F. Frechoso, *Renewable and Sustainable Energy Reviews*, 2013, **28**, 824-835.
38. S. Y. Myong, Y.-C. Park and S. W. Jeon, *Renewable Energy*, 2015, **81**, 482-489.
39. J. Xia, N. Masaki, M. Lira-Cantu, Y. Kim, K. Jiang and S. Yanagida, *J. Am. Chem. Soc.*, 2008, **130**, 1258-1263.
40. C. Jiang, X. Sun, G. Lo, D. Kwong and J. Wang, *Appl. Phys. Lett.*, 2007, **90**, 263501.
41. L.-T. Yan, F.-L. Wu, L. Peng, L.-J. Zhang, P.-J. Li, S.-Y. Dou and T.-X. Li, *International Journal of Photoenergy*, 2012, **2012**.
42. A. Kay and M. Graetzel, *The Journal of Physical Chemistry*, 1993, **97**, 6272-6277.
43. G. Calogero, J.-H. Yum, A. Sinopoli, G. Di Marco, M. Grätzel and M. K. Nazeeruddin, *Solar Energy*, 2012, **86**, 1563-1575.
44. G. Calogero and G. Di Marco, *Sol. Energy Mater. Sol. Cells*, 2008, **92**, 1341-1346.
45. M. K. Nazeeruddin, P. Pechy, T. Renouard, S. M. Zakeeruddin, R. Humphry-Baker, P. Comte, P. Liska, L. Cevey, E. Costa and V. Shklover, *J. Am. Chem. Soc.*, 2001, **123**, 1613-1624.
46. R. Argazzi, G. Larramona, C. Contado and C. A. Bignozzi, *Journal of Photochemistry and Photobiology A: Chemistry*, 2004, **164**, 15-21.
47. G. Calogero, A. Bartolotta, G. Di Marco, A. Di Carlo and F. Bonaccorso, *Chem. Soc. Rev.*, 2015, **44**, 3244-3294.
48. G. Calogero, F. Bonaccorso, O. M. Maragò, P. G. Gucciardi and G. Di Marco, *Dalton Transactions*, 2010, **39**, 2903-2909.
49. *Johnson Matthey Plc., 2012. Platinum 2012*, 2012.
50. B.-K. Koo, D.-Y. Lee, H.-J. Kim, W.-J. Lee, J.-S. Song and H.-J. Kim, *J. Electroceram.*, 2006, **17**, 79-82.
51. A. Agresti, S. Pescetelli, E. Gatto, M. Venanzi and A. Di Carlo, *J. Power Sources*, 2015, **287**, 87-95.
52. e. K. Kalyanasundaram, in *Dye Sensitized Solar Cells*, ed. C. P. EPFL press, Lausanne, Switzerland, Hardcover, 2010, p. 320.
53. H. Wang and Y. H. Hu, *Energy & Environmental Science*, 2012, **5**, 8182-8188.
54. Z. Yin, J. Zhu, Q. He, X. Cao, C. Tan, H. Chen, Q. Yan and H. Zhang, *Advanced Energy Materials*, 2014, **4**, n/a-n/a.
55. Z. Huang, X. Liu, K. Li, D. Li, Y. Luo, H. Li, W. Song, L. Chen and Q. Meng, *Electrochem. Commun.*, 2007, **9**, 596-598.
56. J. E. Trancik, S. C. Barton and J. Hone, *Nano Lett.*, 2008, **8**, 982-987.
57. K. Imoto, K. Takahashi, T. Yamaguchi, T. Komura, J.-i. Nakamura and K. Murata, *Sol. Energy Mater. Sol. Cells*, 2003, **79**, 459-469.
58. A. Peigney, C. Laurent, E. Flahaut, R. Bacsa and A. Rousset, *Carbon*, 2001, **39**, 507-514.
59. R. C. B. J. B. Donnet, M-J. Wang, *Carbon Black Science and Technology*, 1993.
60. H. Marsh and F. R. Reinoso, *Activated carbon*, Elsevier, 2006.
61. C. Lee, X. Wei, J. W. Kysar and J. Hone, *science*, 2008, **321**, 385-388.
62. A. K. Geim and K. S. Novoselov, *Nature materials*, 2007, **6**, 183-191.
63. S. Park and R. S. Ruoff, *Nature nanotechnology*, 2009, **4**, 217-224.

64. F. Bonaccorso, Z. Sun, T. Hasan and A. Ferrari, *Nature photonics*, 2010, **4**, 611-622.
65. X. Wang, L. Zhi and K. Müllen, *Nano Lett.*, 2008, **8**, 323-327.
66. X. Yan, X. Cui, B. Li and L.-s. Li, *Nano Lett.*, 2010, **10**, 1869-1873.
67. L. Britnell, R. Ribeiro, A. Eckmann, R. Jalil, B. Belle, A. Mishchenko, Y.-J. Kim, R. Gorbachev, T. Georgiou and S. Morozov, *Science*, 2013, **340**, 1311-1314.
68. N. Yang, J. Zhai, D. Wang, Y. Chen and L. Jiang, *Acs Nano*, 2010, **4**, 887-894.
69. F. Xu, J. Chen, X. Wu, Y. Zhang, Y. Wang, J. Sun, H. Bi, W. Lei, Y. Ni and L. Sun, *The Journal of Physical Chemistry C*, 2013, **117**, 8619-8627.
70. F. Bonaccorso, N. Balis, M. M. Stylianakis, M. Savarese, C. Adamo, M. Gemmi, V. Pellegrini, E. Stratakis and E. Kymakis, *Adv. Funct. Mater.*, 2015, **25**, 3870-3880.
71. F. Bonaccorso, L. Colombo, G. Yu, M. Stoller, V. Tozzini, A. C. Ferrari, R. S. Ruoff and V. Pellegrini, *Science*, 2015, **347**, 1246501.
72. S. Mathew, A. Yella, P. Gao, R. Humphry-Baker, B. F. Curchod, N. Ashari-Astani, I. Tavernelli, U. Rothlisberger, M. K. Nazeeruddin and M. Grätzel, *Nature chemistry*, 2014, **6**, 242-247.
73. M. J. Ju, J. C. Kim, H.-J. Choi, I. T. Choi, S. G. Kim, K. Lim, J. Ko, J.-J. Lee, I.-Y. Jeon and J.-B. Baek, *ACS nano*, 2013, **7**, 5243-5250.
74. W. Hong, Y. Xu, G. Lu, C. Li and G. Shi, *Electrochem. Commun.*, 2008, **10**, 1555-1558.
75. J. D. Roy-Mayhew, D. J. Bozym, C. Punckt and I. A. Aksay, *Acs Nano*, 2010, **4**, 6203-6211.
76. L. Kavan, J.-H. Yum and M. Graetzel, *ACS Applied Materials & Interfaces*, 2012, **4**, 6999-7006.
77. E. Kymakis, C. Petridis, T. D. Anthopoulos and E. Stratakis, *Selected Topics in Quantum Electronics, IEEE Journal of*, 2014, **20**, 106-115.
78. H. Choi, H. Kim, S. Hwang, W. Choi and M. Jeon, *Sol. Energy Mater. Sol. Cells*, 2011, **95**, 323-325.
79. J. Velten, A. J. Mozer, D. Li, D. Officer, G. Wallace, R. Baughman and A. Zakhidov, *Nanotechnology*, 2012, **23**, 085201.
80. J. Song, Z. Yin, Z. Yang, P. Amaladass, S. Wu, J. Ye, Y. Zhao, W.-Q. Deng, H. Zhang and X.-W. Liu, *Chemistry – A European Journal*, 2011, **17**, 10832-10837.
81. M. Wu, Y. Wang, X. Lin, N. Yu, L. Wang, L. Wang, A. Hagfeldt and T. Ma, *PCCP*, 2011, **13**, 19298-19301.
82. J.-Y. Lin, C.-Y. Chan and S.-W. Chou, *Chem. Commun.*, 2013, **49**, 1440-1442.
83. Y. Hernandez, V. Nicolosi, M. Lotya, F. M. Blighe, Z. Sun, S. De, I. McGovern, B. Holland, M. Byrne and Y. K. Gun'Ko, *Nature nanotechnology*, 2008, **3**, 563-568.
84. K. Novoselov, D. Jiang, F. Schedin, T. Booth, V. Khotkevich, S. Morozov and A. Geim, *Proceedings of the National Academy of Sciences of the United States of America*, 2005, **102**, 10451-10453.
85. B. Brodie, *Ann. Chim. Phys*, 1860, **59**, e472.
86. W. S. Hummers Jr and R. E. Offeman, *J. Am. Chem. Soc.*, 1958, **80**, 1339-1339.
87. C. Mattevi, G. Eda, S. Agnoli, S. Miller, K. A. Mkhoyan, O. Celik, D. Mastrogiovanni, G. Granozzi, E. Garfunkel and M. Chhowalla, *Adv. Funct. Mater.*, 2009, **19**, 2577.
88. J. Hassoun, F. Bonaccorso, M. Agostini, M. Angelucci, M. G. Betti, R. Cingolani, M. Gemmi, C. Mariani, S. Panero and V. Pellegrini, *Nano Lett.*, 2014, **14**, 4901-4906.
89. A. A. Green and M. C. Hersam, *Nano Lett.*, 2009, **9**, 4031-4036.
90. E.G. Acheson, 1896.
91. H. Lipson and A. Stokes, 1942.
92. X. Li, W. Cai, J. An, S. Kim, J. Nah, D. Yang, R. Piner, A. Velamakanni, I. Jung and E. Tutuc, *Science*, 2009, **324**, 1312-1314.
93. S. Bae, H. Kim, Y. Lee, X. Xu, J.-S. Park, Y. Zheng, J. Balakrishnan, T. Lei, H. R. Kim and Y. I. Song, *Nature nanotechnology*, 2010, **5**, 574-578.
94. L. Wang, I. Meric, P. Huang, Q. Gao, Y. Gao, H. Tran, T. Taniguchi, K. Watanabe, L. Campos and D. Muller, *Science*, 2013, **342**, 614-617.
95. K. R. Paton, E. Varrla, C. Backes, R. J. Smith, U. Khan, A. O'Neill, C. Boland, M. Lotya, O. M. Istrate, P. King, T. Higgins, S. Barwich, P. May, P. Puczkarski, I. Ahmed, M. Moebius, H. Pettersson, E. Long, J. Coelho, S. E. O'Brien, E. K. McGuire, B. M. Sanchez, G. S. Duesberg, N. McEvoy, T. J. Pennycook, C. Downing, A. Crossley, V. Nicolosi and J. N. Coleman, *Nat Mater*, 2014, **13**, 624-630.
96. F. Torrisi, T. Hasan, W. Wu, Z. Sun, A. Lombardo, T. S. Kulmala, G.-W. Hsieh, S. Jung, F. Bonaccorso and P. J. Paul, *Acs Nano*, 2012, **6**, 2992-3006.
97. G. Eda, Y.-Y. Lin, C. Mattevi, H. Yamaguchi, H.-A. Chen, I.-S. Chen, C.-W. Chen and M. Chhowalla, *Adv. Mater.*, 2010, **22**, 505.
98. V. Nicolosi, M. Chhowalla, M. G. Kanatzidis, M. S. Strano and J. N. Coleman, *Science*, 2013, **340**, 1226419.
99. D. J. Finn, M. Lotya, G. Cunningham, R. J. Smith, D. McCloskey, J. F. Donegan and J. N. Coleman, *Journal of Materials Chemistry C*, 2014, **2**, 925-932.
100. J. Li, F. Ye, S. Vaziri, M. Muhammed, M. C. Lemme and M. Östling, *Adv. Mater.*, 2013, **25**, 3985-3992.
101. J.-W. T. Seo, A. A. Green, A. L. Antaris and M. C. Hersam, *The Journal of Physical Chemistry Letters*, 2011, **2**, 1004-1008.
102. A. Capasso, A. E. Del Rio Castillo, H. Sun, A. Ansaldo, V. Pellegrini and F. Bonaccorso, *Solid State Commun.*, 2015, **224**, 53-63.
103. A. R. T. M. Brown, A. Di Carlo in *"Organic and Hybrid Solar Cells" in Thin Film Solar Cells: Current Status and Future Trends*, ed. I. Nova Science Publisher, 2011, pp. 249-286.
104. A. Hauch and A. Georg, *Electrochim. Acta*, 2001, **46**, 3457-3466.
105. L. Kavan, J. H. Yum and M. Grätzel, *Acs Nano*, 2010, **5**, 165-172.
106. M. Lotya, Y. Hernandez, P. J. King, R. J. Smith, V. Nicolosi, L. S. Karlsson, F. M. Blighe, S. De, Z. Wang and I. McGovern, *J. Am. Chem. Soc.*, 2009, **131**, 3611-3620.
107. O. M. Maragó, F. Bonaccorso, R. Saija, G. Privitera, P. G. Gucciardi, M. A. Iatì, G. Calogero, P. H. Jones, F. Borghese and P. Denti, *ACS nano*, 2010, **4**, 7515-7523.
108. https://www.sigmaaldrich.com/content/dam/sigma-aldrich/docs/Sigma/Product_Information_Sheet/d4551pis.pdf, (accessed September, 2015).
109. www.lyondellbasell.com/techlit/techlit/2313.pdf.
110. T. P. Svedberg, *The Ultracentrifuge*, 1940.
111. D. Greenaway, G. Harbeke, F. Bassani and E. Tosatti, *Physical review*, 1969, **178**, 1340.

112. V. Kravets, A. Grigorenko, R. Nair, P. Blake, S. Anissimova, K. Novoselov and A. Geim, *Physical Review B*, 2010, **81**, 155413.
113. L. Yang, J. Deslippe, C.-H. Park, M. L. Cohen and S. G. Louie, *Phys. Rev. Lett.*, 2009, **103**, 186802.
114. E. J. Wensink, A. C. Hoffmann, P. J. van Maaren and D. van der Spoel, *The Journal of chemical physics*, 2003, **119**, 7308-7317.
115. A. Einstein, *Investigations on the Theory of the Brownian Movement*, Courier Corporation, 1956.
116. J. C. Meyer, A. K. Geim, M. Katsnelson, K. Novoselov, T. Booth and S. Roth, *Nature*, 2007, **446**, 60-63.
117. A. C. Ferrari and J. Robertson, *Physical review B*, 2000, **61**, 14095.
118. A. C. Ferrari and D. M. Basko, *Nature nanotechnology*, 2013, **8**, 235-246.
119. L. La Notte, D. Mineo, G. Polino, G. Susanna, F. Brunetti, T. M. Brown, A. Di Carlo and A. Reale, *Energy Technology*, 2013, **1**, 757-762.
120. C. Girotto, B. P. Rand, J. Genoe and P. Heremans, *Sol. Energy Mater. Sol. Cells*, 2009, **93**, 454-458.
121. V. H. Pham, T. V. Cuong, S. H. Hur, E. W. Shin, J. S. Kim, J. S. Chung and E. J. Kim, *Carbon*, 2010, **48**, 1945-1951.
122. L. Kavan, J.-H. Yum and M. Graetzel, *Electrochim. Acta*, 2014, **128**, 349-359.
123. L. Kavan, J.-H. Yum and M. Grätzel, *Nano Lett.*, 2011, **11**, 5501-5506.
124. L. Kavan, *Top. Curr. Chem.*, 2014, **348**, 53-93.
125. F. Fabregat-Santiago, J. Bisquert, E. Palomares, L. Otero, D. Kuang, S. M. Zakeeruddin and M. Grätzel, *The Journal of Physical Chemistry C*, 2007, **111**, 6550-6560.
126. S. Sarker, A. Ahammad, H. W. Seo and D. M. Kim, *International Journal of Photoenergy*, 2014, **2014**.
127. Q. Wang, J.-E. Moser and M. Grätzel, *The Journal of Physical Chemistry B*, 2005, **109**, 14945-14953.
128. L. Kavan, J.-H. Yum, M. K. Nazeeruddin and M. Grätzel, *ACS Nano*, 2011, **5**, 9171-9178.
129. J. Yang, C. Bao, K. Zhu, T. Yu, F. Li, J. Liu, Z. Li and Z. Zou, *Chem. Commun.*, 2014, **50**, 4824-4826.
130. F. Gong, H. Wang and Z.-S. Wang, *PCCP*, 2011, **13**, 17676-17682.
131. M. Wu, X. Lin, Y. Wang, L. Wang, W. Guo, D. Qi, X. Peng, A. Hagfeldt, M. Grätzel and T. Ma, *J. Am. Chem. Soc.*, 2012, **134**, 3419-3428.
132. F. Hao, P. Dong, J. Zhang, Y. Zhang, P. E. Loya, R. H. Hauge, J. Li, J. Lou and H. Lin, *Scientific Reports*, 2012, **2**, 368.
133. J. H. Kim, K. J. Moon, J. M. Kim, D. Lee and S. H. Kim, *Solar Energy*, 2015, **113**, 251-257.
134. R. Cruz, J. P. Araujo, L. Andrade and A. Mendes, *Journal of Materials Chemistry A*, 2014, **2**, 2028-2032.
135. M.-Y. Yen, C.-C. Teng, M.-C. Hsiao, P.-I. Liu, W.-P. Chuang, C.-C. M. Ma, C.-K. Hsieh, M.-C. Tsai and C.-H. Tsai, *J. Mater. Chem.*, 2011, **21**, 12880-12888.
136. S. Mastroianni, A. Lanuti, S. Penna, A. Reale, T. M. Brown, A. Di Carlo and F. Decker, *ChemPhysChem*, 2012, **13**, 2925-2936.
137. F. Giordano, A. Guidobaldi, E. Petrolati, L. Vesce, R. Riccitelli, A. Reale, T. M. Brown and A. Di Carlo, *Progress in Photovoltaics: Research and Applications*, 2013, **21**, 1653-1658.